Published in final edited form as:
Mol Imaging Biol. 2012 April ; 14(2): 173–182. doi:10.1007/s11307-011-0494-2.

Optimization of Coded Aperture Radioscintigraphy for Sentinel Lymph Node Mapping

Hirofumi Fujii[1,2], **John D. Idoine**[3], **Sylvain Gioux**[1], **Roberto Accorsi**[4], **David R. Slochower**[1,3], **Richard C. Lanza**[5], and **John V. Frangioni**[1,6,*]

[1]Division of Hematology/Oncology, Beth Israel Deaconess Medical Center, Boston, MA 02215

[2]Functional Imaging Division, National Cancer Center Hospital East, Kashiwa 277-8577 Japan

[3]Department of Physics, Kenyon College, Gambier, OH 43022

[4]Department of Radiology, Children's Hospital of Philadelphia, Philadelphia, PA 19104

[5]Department of Nuclear Engineering, Massachusetts Institute of Technology, Cambridge, MA 02139

[6]Department of Radiology, Beth Israel Deaconess Medical Center, Boston, MA 02215

Abstract

Purpose—Radioscintigraphic imaging during sentinel lymph node (SLN) mapping could potentially improve localization; however, parallel-hole collimators have certain limitations. In this study, we explored the use of coded aperture (CA) collimators.

Procedures—Equations were derived for the six major dependent variables of CA collimators (i.e., masks) as a function of the ten major independent variables, and an optimized mask was fabricated. After validation, dual-modality CA and near-infrared (NIR) fluorescence SLN mapping was performed in pigs.

Results—Mask optimization required the judicious balance of competing dependent variables, resulting in sensitivity of 0.35%, XY resolution of 2.0 mm, and Z resolution of 4.2 mm at an 11.5 cm FOV. Findings in pigs suggested that NIR fluorescence imaging and CA radioscintigraphy could be complementary, but present difficult technical challenges.

Conclusions—This study lays the foundation for using CA collimation for SLN mapping, and also exposes several problems that require further investigation.

[*]**Corresponding Author:** John V. Frangioni, M.D., Ph.D. BIDMC, Room SL-B05 330 Brookline Avenue Boston, MA 02215 Office 617-667-0692; Fax: 617-667-0981 jfrangio@bidmc.harvard.edu.

CONFLICT OF INTEREST STATEMENT
Hirofumi Fujii: None
John D. Idoine: None
Sylvain Gioux: None
Roberto Accorsi: None
David R. Slochower: None
Richard C. Lanza: None
John V. Frangioni, M.D., Ph.D.: All intellectual property for the FLARE™ and m-FLARE™ imaging systems, is owned by the Beth Israel Deaconess Medical Center (BIDMC), a teaching hospital of Harvard Medical School. As inventor of the technology, Dr. Frangioni may someday receive royalties if the technology is ever commercialized. Dr. Frangioni is the founder and unpaid director of The FLARE Foundation, a non-profit organization focused on promoting the dissemination of medical imaging technology for research and clinical use.

Keywords

Coded apertures; coded-aperture collimation; radioscintigraphy; sentinel lymph node mapping; image-guided surgery; near-infrared fluorescence imaging

INTRODUCTION

Intraoperative detection of target tissues is essential for successful surgical treatment. Most often, target tissues are simply identified by visual inspection, which results in low contrast. Radiotracers have been introduced into surgery to provide highly sensitive and specific detection of targets [1]. Sentinel lymph node (SLN) mapping, for example, routinely utilizes ^{99m}Tc-colloids. However, because of inherent collimator limitations, ^{99m}Tc detection is presently performed intraoperatively using a handheld gamma probe. Hence, the target cannot be imaged, but must be found empirically by scanning the surgical field with the small probe and listening for changes in its audible output.

There are presently no radioscintigraphic collimators for intraoperative use that simultaneously provide a large field of view (FOV), high sensitivity, and high resolution. The operating principles of parallel-hole collimators (PHC), pinhole collimators (PC) and multi-pinhole collimators (MPC) are shown in Supplementary Figure 1. A gamma camera fitted with a PHC has relatively high open area; therefore, sensitivity is good, but spatial resolution is poor and cannot be higher than the intrinsic resolution of the detector. In contrast, a gamma camera fitted with a PC shows excellent resolution because the obtained image can be magnified onto the detector. However, sensitivity is low because only a small fraction of gamma rays can pass through the single hole. MPCs increase sensitivity by projecting multiple, non- or slightly overlapping images onto the detector, but FOV is limited and sensitivity is only modest.

A coded aperture (CA; Figure 1a) is a lightweight radio-opaque collimator (i.e., mask) in which multiple holes are arranged in a particular pattern. Unlike MPCs, CAs project multiple overlapping images onto the gamma camera. CAs have features of both PHCs and MPCs, resulting in large FOVs, high sensitivity, and high resolution. Uniquely, CAs provide three-dimensional information about the object from a single view, which is critical in surgery as target depth needs to be known before cutting. Unlike other collimators, though, CAs require that data collection be followed by computer-assisted decoding (Figure 1b) in order to separate the overlapping projections and reconstruct the original object.

The first CA, described by Mertz and Young [2], was the Fresnel zone plate, and was used to observe faint celestial X-ray sources. This CA was composed of alternating radio-opaque and radiolucent rings and has an open area approaching 50%. If the number of rings is quite large (≈ 100), the quality of reconstructed images is excellent. However, the physical size of such a CA would make use in the operating room (OR) difficult. A non-redundant pinhole array [NRPA; [3,4]] is composed of a pattern of 10 to 20 holes, and provides high quality images as its auto-correction function is a delta function with flat side lobes. However, its utility is limited due to an extremely small open area.

In 1978, Fenimore and Cannon [5,6] developed CAs called *uniformly redundant arrays* (URAs), which also achieve the desired delta function response. One of the most important features of an URA is its geometry. If the basic URA is an r (rows) by s (columns) pattern, successful reconstruction with minimal artifacts can be performed for a 2r by 2s mosaicked aperture. Another feature of an URA is that its open fraction can be as high as 30% to 50%.

Thus, URAs combine the high sensitivity of Fresnel zone plates with the improved point spread function (PSF) of NRPAs.

On the basis of these promising results, clinical application of CAs was investigated in the early 1980s [7,8], but interest waned because of the complexity of decoding, and the presence of artifacts whenever objects were close to the CA mask. By 2001, however, computing power had improved significantly, and a simple 90° mask rotation algorithm was found to virtually eliminate near-field artifacts [9]. Although proof of principle for using CA in medical imaging has been reported [10,11], there has yet to be a systematic study of the multiple independent variables that affect CA collimator performance. In this study, we hypothesized that SLN mapping, an important cancer surgery that is most similar to a "bright star on a black background," might benefit from CA collimation.

MATERIALS AND METHODS

Coded Aperture Mask and Gamma Camera

See Supplementary Material and Supplementary Figures 2-7 for a detailed description of CA theory. CA masks were fabricated from 7.2" × 19" sheets of Kulite-1750 (H.C. Starck, Inc., East Rutherford, NJ), a tungsten alloy having a density of 17.5 g/cm^3 and a composition of 92.5% tungsten, 3.0% nickel, 2.0% copper and 2.5% iron. The total attenuation coefficient for 140 keV ^{99m}Tc photons was 31.83 cm^{-1}. After cutting to the desired size using a brake, holes were drilled by QC Drilling (Salem, NH) based on a Gerber file pattern created using custom software written in MATLAB (MathWorks, Natick, MA). Custom LabVIEW software (National Instruments, Austin, TX) was written to predict CA mask performance as a function of all independent variables. The optimized CA mask derived from this software, and used for all experiments, had the following parameters: hole diameter $\boldsymbol{Pa}$ = 1.45 mm, number of pixel positions per mask period $\boldsymbol{npm}$ = 62, and mask side $2\boldsymbol{d}$ = 18.0 cm. Mask thickness ($\boldsymbol{mt}$) was 1 mm, resulting in 4.2% transmission of 140 keV photons through the opaque portion of the mask.

The detector was a SMART Digital Detector (Scandia Corporation, Urbandale, IA) with a ½" NaI scintillator, a total FOV of 41.9 cm × 56.6 cm, an effective short dimension ($\boldsymbol{D}$) of 40 cm, and an intrinsic resolution ($\boldsymbol{IR}$) of 3 mm. The center of the CA mask was positioned $\boldsymbol{b}$ = 35 cm from the center of the scintillation crystal, and the object-to-mask distance ($\boldsymbol{a}$) was varied from 10 to 40 cm as indicated. The energy window for ^{99m}Tc was set at 126 to 154 keV (140 keV ± 10%) to minimize counting of scattered photons. Photopeak detection efficiency ($\boldsymbol{PDE}$) of the detector for 140 keV photons was 93%. An aluminum, truncated pyramid-shaped frame permitted mounting of the mask on a rotary bearing (Catalog #18635A52, McMaster-Carr, Atlanta, GA,), as well as mounting of ¼" lead-antimony shielding to protect the detector from scattered photons.

Image Acquisition, Decoding, and Reconstruction

Images were acquired with a detector pixel size ($\boldsymbol{dp}$) of 1.344 mm (311 pixels total for the 41.9 cm detector) and stored in a 512 × 512 matrix with unused positions padded with zeroes. To eliminate the near-field artifact arising during the laminographic reconstruction of images, an anti-mask image was acquired by rotating the CA mask 90° [9]. Acquired data corresponding to the central $\boldsymbol{d} \times \boldsymbol{d}$ region of the mask (see Supplementary Material) were decoded and reconstructed by Fourier deconvolution (laminography) using a MATLAB program described previously [12].

To obtain reliable results during laminography, the sampling index, defined as the ratio of the size of the mask pixel projection on the detector to the detector pixel size ($\boldsymbol{dp}$), must ≥ 2

[12]. Sampling index is calculated by $\frac{Pa \times M}{dp}$. Laminographic image reconstruction was employed as described previously [9].

Measurement of Field of View (FOV), Sensitivity, and Resolution

^{99m}Tc point sources measuring 75-μm in diameter loaded with the activity indicated were prepared as described previously [13]. See Supplementary Material and Supplementary Figure 3 for a detailed description of the experimental setups and equations used to measure FOV, sensitivity, XY resolution, and Z resolution of CA masks.

Combined CA Radioscintigraphy and Near-infrared (NIR) Fluorescence Imaging for Sentinel Lymph Node (SLN) Mapping of Pigs

The first generation Fluorescence-Assisted Resection and Exploration (FLARE™) imaging system used in this study has been described in detail previously [14]. The imaging head was attached to the gamma camera using a rigid, 4" thick, extruded aluminum post (Parker Industrial Profile Systems, Marlborough, MA). Alignment, co-registration, and calibration of the optical and nuclear imaging sub-systems were performed using 1 mm styrene-divinylbenzene beads co-labeled with NIR fluorophore indocyanine green and ^{99m}Tc-pertechnetate [15].

Yorkshire pigs (E.M. Parsons & Sons, Hadley, MA) weighing 35 kg were used under the supervision of an approved institutional protocol. Anesthesia was induced with 4.4 mg/kg intramuscular Telazol™ (Fort Dodge Labs, Fort Dodge, IA) and maintained after intubation with 2% isoflurane/balance O_2. Two hundred microliters of a mixture of lymphatic tracers in saline were injected into the parenchyma of the colon as described in detail previously [16]. This mixture consisted of 4.07 MBq (110 μCi) ^{99m}Tc-albumin [17] and 10 μM NIR fluorescent albumin [HSA800; [18]]. The distance ***b*** between mask and detector was fixed at 35 cm. The minimal distance from mask to object (min ***a***) was 10 cm (i.e., the operating room table thickness). The injection site and SLN were imaged *in vivo* at ***a*** ≈ 25 cm. *Ex vivo*, the SLN was imaged at ***a*** ≈ 10 cm.

RESULTS

Incorporation of Mask Thickness into the Equations Describing FOV, Sensitivity, and Resolution

In most CA studies, mask thickness (***mt***) is assumed to be infinitesimally thin, and the key dependent variables FOV, sensitivity, XY resolution, and Z resolution can be described by the analytical equations provided in Supplementary Table 1. However, even when using high-density alloys such as Kulite-1750, mask thickness (***mt***) must be finite in order to minimize non-hole transmission. The geometrical effect of ***mt*** on photon penetration is detailed in Figure 1c, and provides an analytical framework to modify dependent variable equations to take ***mt*** into account (Table 1). Of note, two possible equations now exist for FOV, depending on the relationship between ***a, b***, and ***mt*** (Supplementary Figure 2). The equation for Z-resolution has not been modified to include ***mt***, as this modification would require a numerical, rather than an analytical solution.

The Influence of Ten Key Independent Variables on FOV, Sensitivity, and Resolution

We systematically probed how changes in the ten independent variables (Figure 1d) of CA imaging systems (Table 1) affected the key dependent variables (FOV, sensitivity, and resolution) that define CA performance. Using custom software, a single independent variable was changed while all others were held constant. A "valid" FOV could be obtained

only when certain complex conditions were met (Supplementary Table 2); therefore, the independent variables ***a, b, npm***, and ***Pa*** were constrained to particular ranges (Table 2).

To test the predictive power of our analytical equations, with and without the incorporation of ***mt***, we performed systematic variation of ***a*** using the experimental setups described in Materials and Methods and Supplementary Material. As shown in Figure 2, incorporation of the geometrical effect of ***mt*** into the equations improved the prediction of sensitivity when ***a*** was small, and XY resolution when ***a*** was large. As might be expected by the relative differences in scale, FOV was unaffected by ***mt***, provided that all other parameters were set to produce a "valid" FOV.

In Silico Optimization of CA Masks

Using these equations, we systematically varied ***a, b, npm, Pa***, and ***D*** to determine their effect on FOV, sensitivity, XY resolution, and Z resolution. The figure of merit used to optimize CA performance was the ratio of sensitivity to the square of XY resolution $\left(=\frac{Sensitivity}{(XY\_resolution)^2}\right)$, which is proportional to the signal to noise ratio (SNR; see below and Supplementary Material). Additionally, the following three conditions were met: (1) $d \times \frac{a+b}{a+\frac{mt}{2}} \leq D$, (2) the sampling index was larger than 2 when ***a*** was 10 – 40 cm, and (3) ***npm*** was small enough for the gamma rays required for image reconstruction to pass through the mask at min ***a*** = 10 cm. Of note, for a fixed mask size 2***d***, a large ***npm*** forces a small hole diameter ***Pa***, which thus limits the effective hole area.

As shown in Figure 3 and summarized in Table 3, the relationships among the variables were complex and subject to inherent tradeoffs. From an image-guided surgery perspective, the results revealed a troubling trend: CA mask sensitivity and resolution deteriorated rapidly as the object-to-mask distance ***a*** was increased or detector width ***D*** was decreased.

Nevertheless, we were able to use these data to design "optimized" CA masks for ^{99m}Tc-based SLN mapping. Because operating room tables have a finite thickness, this defines a "minimum ***a***" (min ***a***), which is typically 10 cm. Patients also have a finite thickness and surgery is typically performed from above; therefore, we optimized all masks at ***a*** = 25 cm (min ***a*** + 6"; where 6" is the mid-point of the torso for an adult). The results, summarized in Table 4, reveal that CA masks for SLN mapping can have a simultaneously large FOV, high sensitivity, and high resolution, provided that D is as large as possible. Once again, though, CA mask performance is highly dependent on ***a***. Performance is also highly-dependent on the object size, and as described in detail in Supplementary Material, Supplementary Figure 7, and Supplementary Table 3, there is a troubling trend where SNR falls off dramatically as object size increases (i.e., becomes more distributed).

In Vivo Characterization of Optimized CA Mask Performance

Although our analytical equations (Table 1) predicted CA mask performance (Figure 2) and permitted optimization of FOV, sensitivity, and resolution (Figure 3 and Table 4), the effect of object size (Supplementary Figure 7 and Supplementary Table 3) suggested that *in vivo* imaging might be problematic. Bone scanning with ^{99m}Tc-MDP provided a model system in which both point source-like objects (e.g., knee joints, shoulder joints) and distributed objects (e.g., spine, skull) exist in the same study subject. The results shown in Supplementary Figure 8 demonstrate the pros and cons of CA imaging *in vivo*. Resolution of point source-like objects (i.e., knee joints) can be excellent, but such bright objects constrain the dynamic range available to the rest of the image. Moreover, distributed objects such as

the spine and skull are very poorly resolved (see Discussion), even when laminographic reconstruction is performed at a level where they should be.

Simultaneous Optical/Nuclear SLN Mapping in Large Animals Approaching the Size of Humans

In vivo results with mice bone scanning suggested that the best-case scenario for CA-based image-guided surgery would be in a procedure with a low background and a point source-like object. SLN mapping provides such conditions because radioisotope is injected locally, and the SLN is typically ≤ 1 cm in diameter. To provide an internal gold standard for imaging and surgical landmarks, an image-guided surgery system was constructed that permitted simultaneous acquisition of color video, NIR fluorescence, and CA radioscintigraphy (Figure 4a). When a mixture of radioactive and NIR fluorescent lymphatic tracers were injected into pig colon, the pros and cons of each technique became readily apparent. If the lymphatic channel dived under the mesentery and the SLN was below bowel, the NIR fluorescent signal was lost (Figure 4b). The CA signal from the SLN was reconstructable under all conditions, but only if the initial injection site was blocked by lead placed between it and the CA mask. CA imaging also provided limited Z resolution, i.e., depth information (Figure 4c). The activity in the SLN was approximately 2% of the total injected activity. After image-guided resection of a group of mesenteric lymph nodes, both NIR and CA radioscintigraphic signals were found to co-localize in the SLN (Figure 4d).

DISCUSSION

To the best of our knowledge, this is the first study to define all of the key dependent and independent variables of CA imaging, incorporate mask thickness into readily solved analytical equations, define the valid ranges for each independent variable as a function of detector size, and optimize CA masks for SLN mapping. Although we were able to construct an “optimized” mask for use on human sized subjects in an operating room setting, as well as construct a hybrid NIR-fluorescence/radioscintigraphic imaging system, our results with SLN mapping in large animals exposed several problems that may or may not be surmountable.

First, SLN mapping will often require the orientation of the CA imaging system anywhere in three-dimensional space. Due to the weight and bulk of our CA mask/detector/shielding combination, and rigid attachment to the FLARE™ imaging system, we were only able to image using the detector in the “upward facing” orientation. We found this to be problematic due to the difficulty in shielding the injection site during SLN mapping, difficulty in positioning the subject relative to the imaging system, and loss of photons from attenuation by the body. New, more compact, solid-state gamma cameras might provide more agile positioning, but care must be taken in properly shielding the detector from stray and scattered photons, and inherent resolution of the detector must remain high. Also, as summarized in Table 4 and Figure 3, one needs relatively large detectors (***D***) in order to achieve useful clinical FOVs. For example, a 30-cm detector is required to achieve ≈ 11 cm FOV, and increasing ***D*** improves Z resolution significantly.

Second, due to their profound influence on mask performance, the object-to-mask distance ***a*** and the object to detector distance (***a*** + ***b***) should be adjustable under computer control. It is likely that “scanning” in the Z-direction may be necessary to improve depth resolution and to ensure that low activity lesions are detectable.

Third, the “concentration effect” is, potentially, the fatal flaw of CA-based SLN mapping. CAs were initially developed by astrophysicists to see bright stars on a black background. One of the reasons they are so effective is that all photons passing through the mask holes

will hit the detector. However, once the source changes from a concentrated point source to a diffuse source, the noise on the detector increases substantially. And, in general, a single high activity object (point source or diffuse) within the surgical field will severely constrain the dynamic range of the system to below ≈ 5 to 10, thus making even moderate activity objects invisible. This is exactly what we saw during SLN mapping in the pig, where the 2% (1:50 dynamic range) of injected activity accumulating in the SLN was invisible until the injection site was shielded (data not shown). Such a limitation on dynamic range makes it even more unlikely that non-SLN applications, such as tumor resection using an intravenously injected targeted agent, would be possible as small collections of tumor cells could be rendered invisible by even low levels of diffuse uptake in surrounding normal tissues and organs.

Fourth, the loss of dynamic range due to the concentration effect will adulterate the image of the "true" object. As shown during mouse bone scanning (Supplementary Figure 8), the spine and skull are poorly resolved, likely due to their distributed nature and the presence of bright point sources (knee joints) that constrain dynamic range. Our results are consistent with previous reports of bone scanning in mice using CA [11], and dims the prospects for quantitative imaging using CA systems.

Fifth, higher photon energies will require thicker masks with reduced performance. Using Kulite-1750, the highest density material available to us, 1 mm of thickness corresponded to a ≈ 96% stopping power for 140 keV ^{99m}Tc photons. Similar stopping power for the 245 keV photon of ^{111}In would require a mask of ≈ 4 mm thickness. This would cause mask "holes" to become cylinders and would negatively affect all key dependent variables. Preliminary studies (data not shown) suggest that the reconstruction algorithms are more tolerant than expected of excess noise from non-hole mask transmission; however, future studies should determine, precisely, the tolerance of reconstruction algorithms for added noise on the detector, and the ability to subtract background counts prior to decoding.

Sixth, Z resolution using standard laminographic reconstruction is rather poor, and falls off quickly as $\boldsymbol{a}$ increases. What role iterative reconstruction algorithms, 3-D (i.e., rotational) data acquisition, or alternative mask patterns to the NHTH MURA, will play in improving Z resolution remains to be seen.

And, finally, as shown in Figure 4, the combination of optical imaging (color video and NIR fluorescence) and coded aperture radioscintigraphy appear to complement each other. The former provides real-time, high-resolution imaging of near-surface objects, while the latter provides high-sensitivity, moderate resolution of deep objects.

CONCLUSIONS

Our study lays the foundation for designing CA masks for SLN mapping and defines the complex tradeoffs among independent variables. Although the "concentration effect" has been exposed as a major obstacle that requires complete shielding of the injection site, our study also proves the principle that optical (i.e., NIR fluorescence) and nuclear (i.e., CA radioscintigraphy) sub-systems are complementary.

Supplementary Material

Refer to Web version on PubMed Central for supplementary material.

Acknowledgments

We thank Elaine P. Lunsford of the Longwood Small Animal Imaging Facility for assistance with image display, Preeti Misra for preparation of ^{99m}Tc- albumin, Hak Soo Choi for preparation of HSA800, J. Anthony Parker for many helpful discussions, Mary McCarthy, Lorissa A. Moffitt, and Lindsey Gendall for editing, and Eugenia Trabucchi for administrative assistance. This work was supported by National Institutes of Health (NIH) grant R01-CA-115296 (JVF) and grants from the Lewis Family Fund (JVF) and the Ellison Foundation (JVF).

REFERENCES

1. Fujii H, Kitagawa Y, Kitajima M, Kubo A. Sentinel nodes of malignancies originating in the alimentary tract. Ann. Nucl. Med. 2004; 18:1–12. [PubMed: 15072178]
2. Mertz, L.; Young, NO. The International Conference on Optical Instruments and Techniques. Vol. 305. Chapman and Hall; London: 1961. Fresnel transformation of images..
3. Chang L, MacDonald B, Ferez-Mendez V, Shiraishi L. Coded aperture imaging of gamma-rays using multiple pinhole arrays and multiwire proportional chamber detector. IEEE Trans. Nucl. Sci. 1975; 22:374–378.
4. Golay MJE. Point arrays having compact, nonredundant autocorrelations. J. Opt. Soc. Am. 1971; 61:272–273.
5. Fenimore E. Coded aperture imaging: predicted performance of uniformly redundant arrays. Appl. Opt. 1978; 17:3562–3570. [PubMed: 20204031]
6. Fenimore EE, Cannon TM. Coded aperture imaging with uniformly redundant arrays. Appl. Opt. 1978; 17:337–347. [PubMed: 20174412]
7. Resinger WW, Rose EA, Keyes JW Jr. et al. Tomographic thyroid scintigraphy: comparison with standard pinhole imaging: concise communication. J. Nucl. Med. 1981; 22:638–42. [PubMed: 6973011]
8. Rogers WL, Koral KF, Mayans R, et al. Coded-aperture imaging of the heart. J. Nucl. Med. 1980; 21:371–8. [PubMed: 6966679]
9. Accorsi R, Lanza RC. Near-field artifact reduction in planar coded aperture imaging. Appl. Opt. 2001; 40:4697–705. [PubMed: 18360511]
10. Accorsi R, Gasparini F, Lanza R. A coded aperture for high-resolution nuclear medicine planar imaging with a conventional Anger camera: experimental results. IEEE Trans. Nucl. Sci. 2001; 48:2411–2417.
11. Schellingerhout D, Accorsi R, Mahmood U, Idoine J, Lanza RC, Weissleder R. Coded aperture nuclear scintigraphy: a novel small animal imaging technique. Mol. Imaging. 2002; 1:344–53. [PubMed: 12926230]
12. Accorsi, R. Ph.D. Thesis. Dept. of Nuclear Engineering, MIT; Cambridge: 2001. Design of a near-field coded aperture cameras for high-resolution medical and industrial gamma-ray imaging..
13. English JR, Accorsi R, Idoine JD, et al. Sub-millimeter technetium-99m calibration sources. Mol. Imaging Biol. 2002; 4:380–4. [PubMed: 14537114]
14. De Grand AM, Frangioni JV. An operational near-infrared fluorescence imaging system prototype for large animal surgery. Technol. Cancer. Res. Treat. 2003; 2:553–62. [PubMed: 14640766]
15. De Grand AM, Lomnes SJ, Lee DS, et al. Tissue-like phantoms for near-infrared fluorescence imaging system assessment and the training of surgeons. J. Biomed. Opt. 2006; 11:014007. [PubMed: 16526884]
16. Soltesz EG, Kim S, Kim SW, et al. Sentinel lymph node mapping of the gastrointestinal tract by using invisible light. Ann. Surg. Oncol. 2006; 13:386–96. [PubMed: 16485157]
17. Misra P, Lebeche D, Ly H, et al. Quantitation of CXCR4 expression in myocardial infarction using 99mTc-labeled SDF-1alpha. J. Nucl. Med. 2008; 49:963–9. [PubMed: 18483105]
18. Ohnishi S, Lomnes SJ, Laurence RG, Gogbashian A, Mariani G, Frangioni JV. Organic alternatives to quantum dots for intraoperative near-infrared fluorescent sentinel lymph node mapping. Mol. Imaging. 2005; 4:172–81. [PubMed: 16194449]

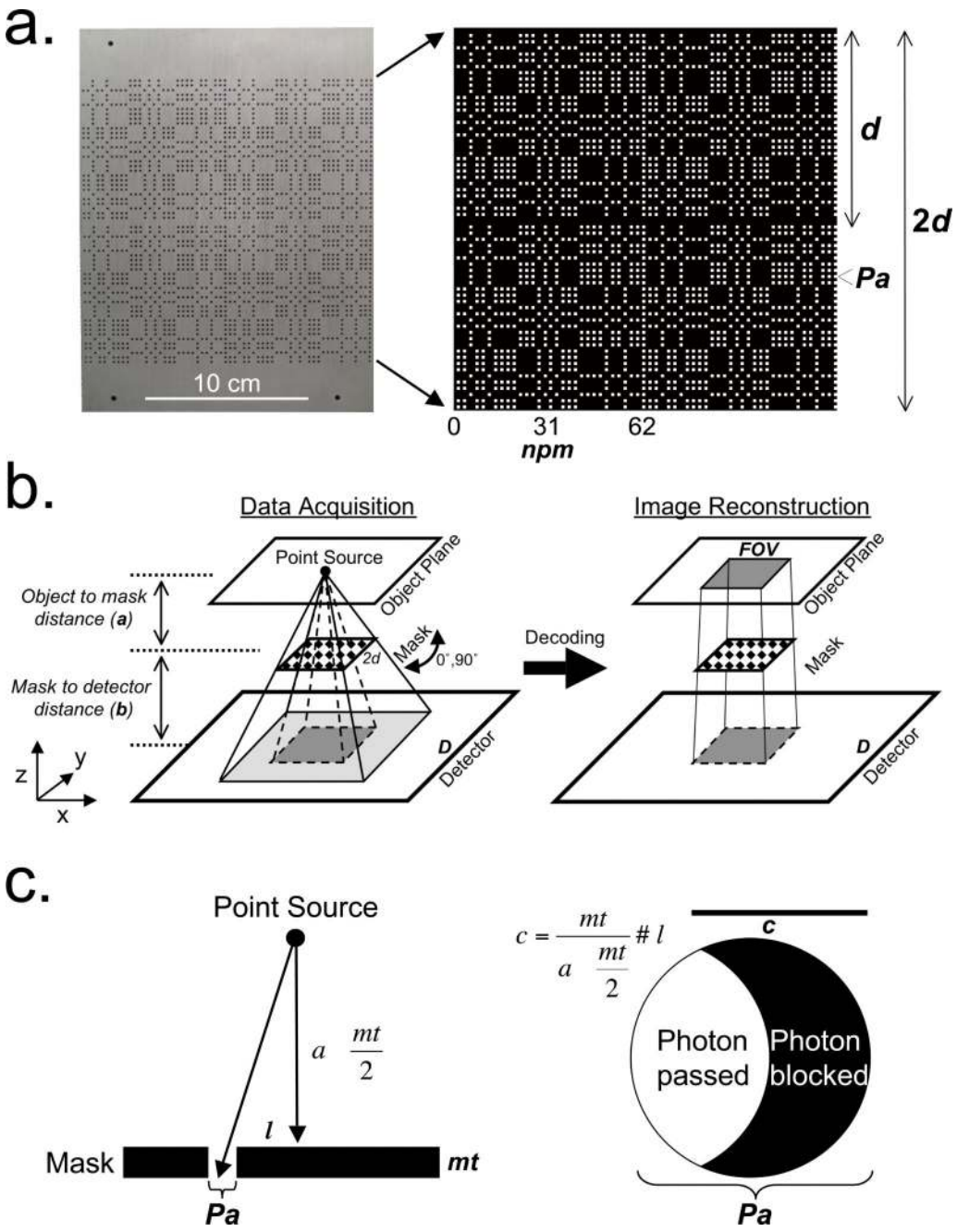

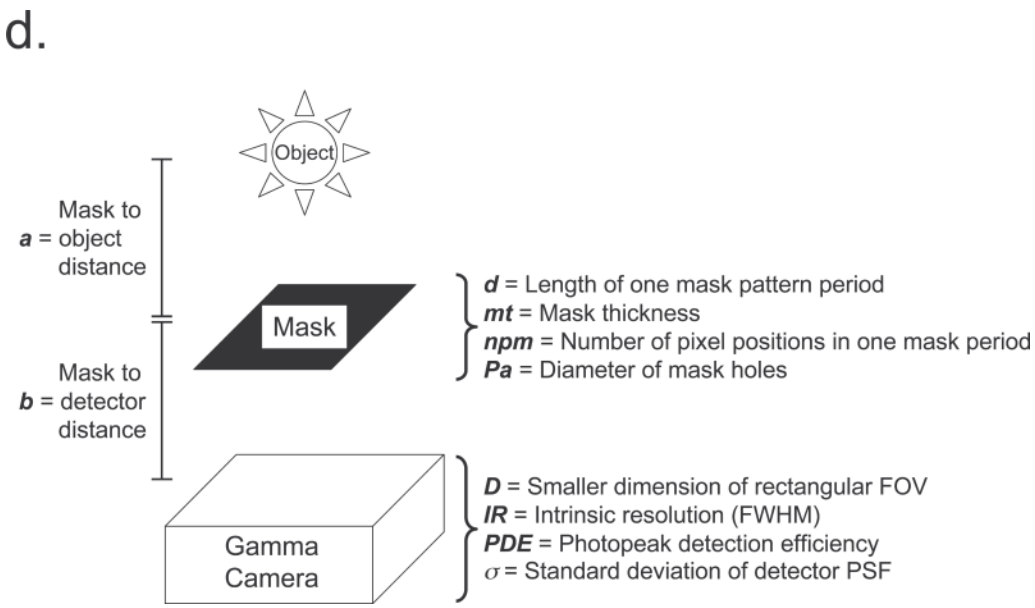

Figure 1. Principles of coded aperture radioscintigraphy

a. Radio-opaque Kulite-1750 mask (left) having a repeating, no-two-holes touching (NTHT), modified uniform redundant array (MURA) pattern of ***npm*** (= 62) open and closed round holes (right). Each hole has a diameter of ***Pa*** (= 1.45 mm). The repeating square pattern has a length of ***d*** (= 9 cm), and the overall mask has a length of 2***d*** (= 18 cm).

b. The object-to-mask distance (***a***) and the mask-to-detector distance (***b***) define the magnification of the mask pattern (light gray), and central ***d*** area of the mask pattern (dark gray), onto the detector after illumination from a point source. Data are decoded through deconvolution, resulting in the formation of an image within a finite FOV on the object plane.

c. Mask thickness and its geometrical effect on photon transmission. As shown, gamma rays from a point source can only pass through the open area of the each hole, with the blocked area (***c***) derived from the equation shown.

d. Schematic summary of the ten key independent variables of coded aperture imaging.

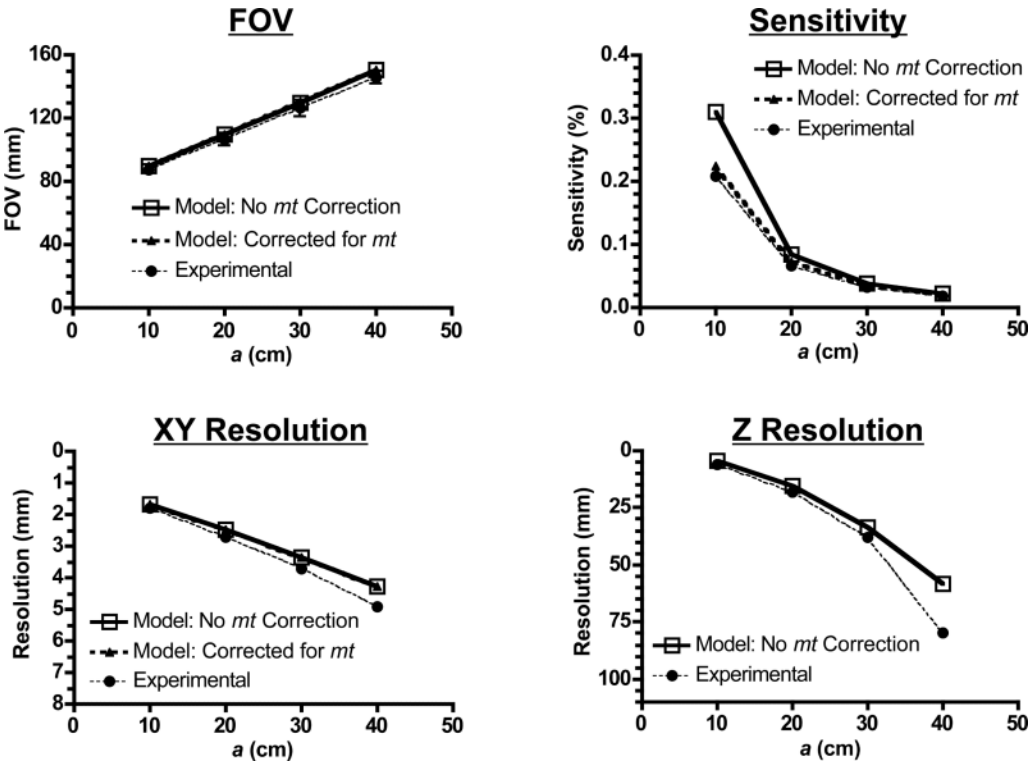

Figure 2. The dependent variables FOV, sensitivity, XY resolution, and Z resolution as a function of the object-to-mask distance *a*

Shown are theoretical (model) values, with and without correction for mask thickness (***mt***), as well as experimental values using a 75 μm diameter ^{99m}Tc point source of uniform activity. The default values for each independent variable were: ***a*** = 20 cm, ***b*** = 25 cm, ***npm*** = 62, and ***Pa*** = 1.44 mm. ***a*** was varied from 1 to 60 cm, in 1 cm increments. ***b*** was varied from 5 to 100 cm, in 5 cm increments. ***npm*** was varied using numbers for which anti-symmetric NTHT MURA patterns exist and valid results can be obtained under the condition that ***a*** = 20 cm, ***b*** = 25 cm and ***mt*** = 1 mm. Such values were 2, 6, 14, 22, 38, 46, 62, 86, 94, 118, 134 and 142. ***Pa*** was varied from 0.4 to 3.0 mm, in 0.1 mm increments.

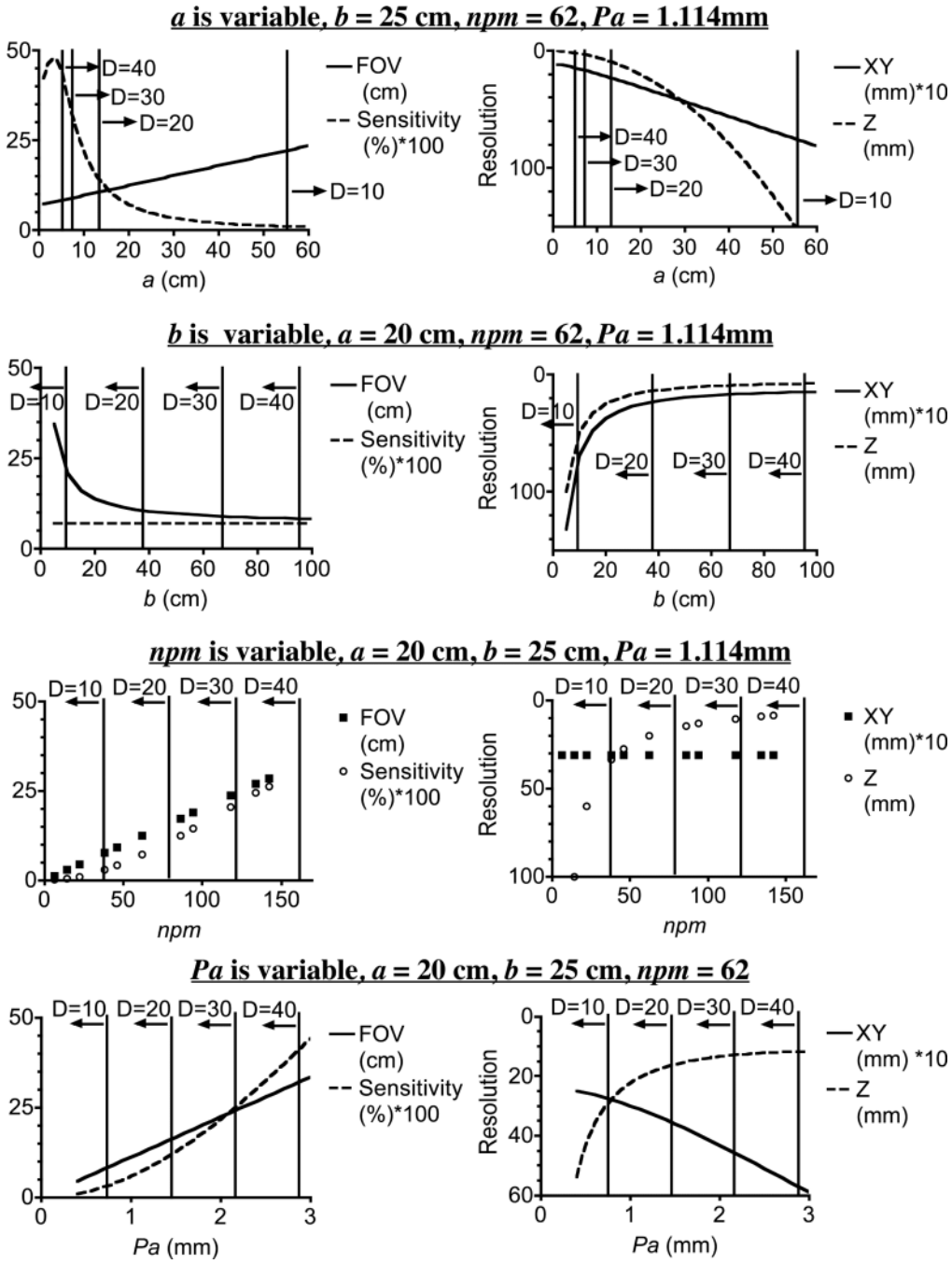

Figure 3. Optimization of coded aperture mask performance using sensitivity/(XY resolution)^2 as the figure of merit

Shown are the results obtained by varying the key independent variables ***a*** (top row), ***b*** (second row), ***npm*** (third row) and ***Pa*** (bottom row). Also indicated are the regions of each curve (arrows) that are valid for various square detectors having length ***D*** (in cm). To save space, FOV (cm) and sensitivity (%*100) are shown on each left graph and XY resolution (mm*10) and Z resolution (mm) are shown on each right graph.

a.

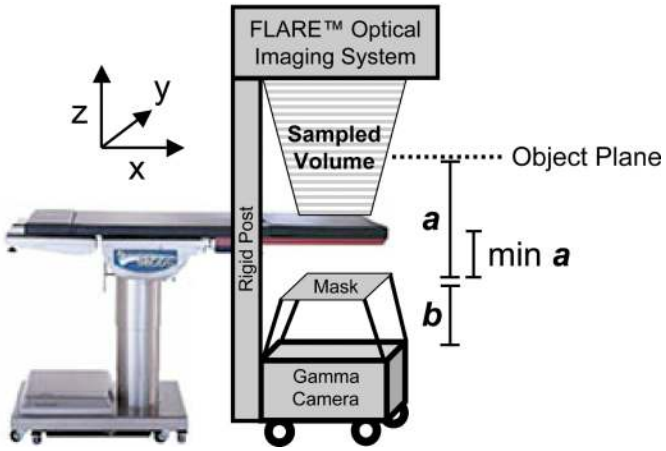

b.

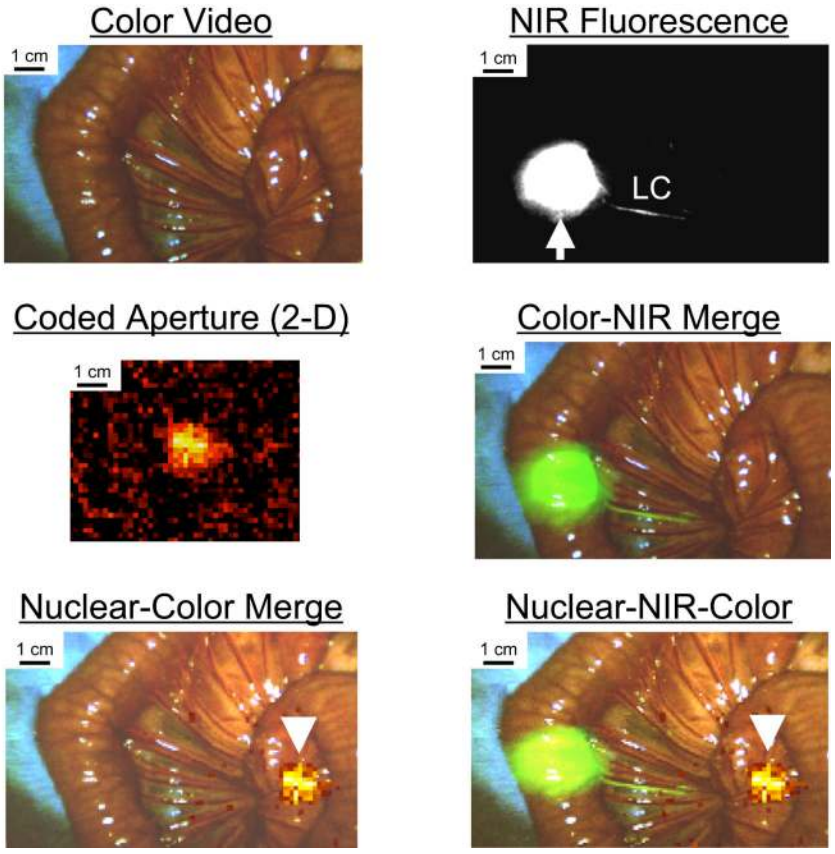

c.

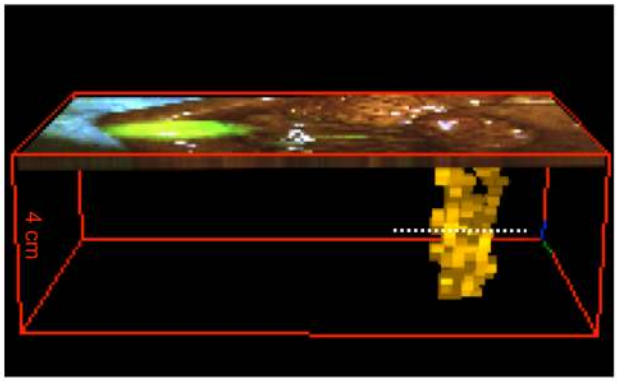

d.

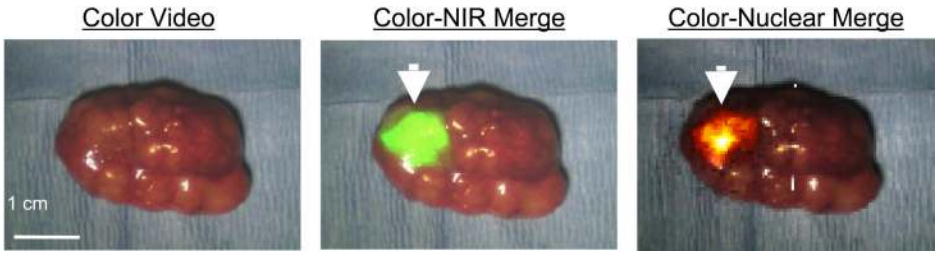

Figure 4. Simultaneous coded aperture radioscintigraphy and NIR fluorescence for SLN mapping

a. Experimental apparatus comprised of the FLARE™ NIR fluorescence image-guided surgery system connected through a rigid post to a CA imaging system. The minimal usable distance (min ***a***) is defined by the height of the operating room tabletop relative to the mask.

b. Image-guided SLN mapping of pig colon. A mixture of ^{99m}Tc-albumin (4.07 MBq; 110 μCi) and NIR fluorescent HSA800 (10 μM) was injected into the parenchyma of pig colon. Shown are individual and merged images for color video, NIR fluorescence, laminographic (i.e., planar) coded aperture reconstruction centered over the SLN, and various 2-D merges of each. Arrow and arrowhead indicate injection site and SLN, respectively. Lymphatic channels (LC) are visible using NIR fluorescence. ***a*** = 25 cm (min ***a*** = 10 cm). Results are representative of n = 3 independent experiments.

c. 3-D merge of all optical and nuclear data, with thresholding of coded aperture data to lower noise. Dashed white line represents plane of the laminographic reconstruction shown in (b).

d. Post-resection analysis of mesenteric lymph nodes. Resection of the lymph node group guided by Figures 4b and 4c and identification of the SLN (arrowheads) using optical and nuclear imaging.

Table 1

Key Independent and Dependent Variables in Coded Aperture Imaging Taking into Account the Geometrical Effect of Mask Thickness.

Independent Variables	
a	Mask to object distance
b	Mask to detector distance
d	Length of one period of mask (= $npm \times P_a$)
D	The smaller dimension of the rectangular FOV of the detector
IR	Intrinsic resolution (FWHM) of camera (= 3 mm for the camera used in this study)
mt	Mask thickness
npm	Number of pixel positions (open or closed) in one mask period
P_a	Diameter of mask holes
PDE	Photopeak detection efficiency of detector
σ	Standard deviation of the Gaussian representing the intrinsic PSF of the camera ($= \frac{IR}{2\sqrt{2 \times \ln 2}} = 1.274$ mm for the camera used in this study). Note that $\frac{1}{2\sqrt{2 \times \ln 2}}$ is the classic conversion factor from FWHM to standard deviation.

Dependent Variable	**Formula**	**Notes**
Magnification of object on detector (*m*)	$\frac{b}{a}$	
Magnification of mask on detector (*M*)	$\frac{a+b}{a+\frac{mt}{2}}$	
FOV		Only valid if:
1) Mask length ≤ Image on the detector ($a \le b$ - *mt*)	$\frac{(a+b)}{b-\frac{mt}{2}} \times d$	$d \times \frac{a+b}{a+\frac{mt}{2}} \le D$ and $npm < \frac{\sqrt{2}\left(a+\frac{mt}{2}\right)\left(b-\frac{mt}{2}\right)}{mt(a+b)}$
2) Mask length > Image on the detector ($a > b$ - *mt*)	$\frac{(a+b)\left(a+\frac{3}{2}mt\right)}{\left(a+\frac{mt}{2}\right)\left(b+\frac{mt}{2}\right)} \times d \; (a > b\text{-}mt)$	$d \times \frac{a+b}{a+\frac{mt}{2}} \le D$ and $npm < \frac{\sqrt{2}\left(a+\frac{mt}{2}\right)\left(b+\frac{mt}{2}\right)}{(2mt+a+b)mt}$
XY Resolution	$\sqrt{\left(IR \times \frac{a}{b}\right)^2 + \left[\frac{Pa \times a(a+b)}{\left(a+\frac{mt}{2}\right)\left(b+\frac{mt}{2}\right)}\right]^2}$	

Dependent Variable	Formula	Notes
Z Resolution	$\frac{4 \times (npm-1) \times a \times \left(\frac{a}{b} \times \frac{X_c}{P_a}\right)}{(npm-1)^2 - 4 \times \left(\frac{a}{b} \times \frac{X_c}{P_a}\right)^2}$	X_c is the positive solution of analytical equation (1) described in the footnotes. There is no correction for mask thickness as this would require a numerical solution.

Sensitivity	See formula (2)
(1)	$\frac{\sigma^2}{2X_c^2}\left[E_+ \times erf(E_+) - E_- \times erf(E_-) + \frac{1}{\sqrt{\pi}}\exp\left(-E_+^2\right) - \frac{1}{\sqrt{\pi}}\exp\left(-E_-^2\right)\right]^2 = k \times erf^2\left[\frac{M \times P_a \times f}{2 \times \sqrt{2} \times \sigma}\right]$, where: $E_+ = \frac{\left(\frac{M \times P_a \times f}{2} + X_c\right)}{\sqrt{2} \times \sigma}$, $E_- = \frac{\left(\frac{M \times P_a \times f}{2} - X_c\right)}{\sqrt{2} \times \sigma}$ and $erf(x) = \frac{2}{\sqrt{\pi}}\int_0^x \exp\left(-t^2\right)dt$
(2)	$\frac{\rho_{ap}}{8\pi}\int_{-npm/2}^{npm/2}\int_{-npm/2}^{npm/2}\frac{Pa^2 A}{\left(Pa^2 x^2 + Pa^2 y^2 + A^2\right)^{3/2}}\left[\arccos\left(\frac{mt}{A}\sqrt{x^2+y^2}\right) - \frac{mt}{A}\sqrt{x^2+y^2}\sqrt{1-\left(\frac{mt}{A}\right)^2\left(x^2+y^2\right)}\right]dxdy * PDE$, where: $A = a - \frac{mt}{2}$ and $\rho_{ap} = \pi \times \frac{\left(\frac{npm^2}{4} - 1\right)}{8 \times npm^2}$ (Open area fraction of aperture for round mask hole)

Table 2

The Range of Each Independent Variable to Obtain a Valid FOV for Square Detectors of Various Lengths.

	Detector Size			
Independent Variable	***D* = 10 cm**	***D* = 20 cm**	***D* = 30 cm**	***D* = 40 cm**
a (cm)	$a \geq 55.7$	$a \geq 13.1$	$a \geq 7.41$	$a \geq 5.16$
b (cm)	$b \leq 9.03$	$b \leq 38.1$	$b \leq 67.1$	$b \leq 96.1$
npm	$npm \leq 38$	$npm \leq 62$	$npm \leq 118$	$npm \leq 142$
Pa (mm)	$Pa \leq 0.72$	$Pa \leq 1.44$	$Pa \leq 2.16$	$Pa \leq 2.87$

Table 3

Summary of the Effects of Each Independent Variable on the Key Dependent Variables of Coded Aperture Imaging.

	Dependent Variables				
Independent Variable	**Change**	**FOV**	**XY Resolution**	**Z Resolution**	**Sensitivity**
a (object-to-mask distance)	Increased	Increased	Deteriorated	Deteriorated	Deteriorated
b (mask-to-detector distance)	Increased	Decreased	Improved	Improved	No change
npm (number of pixel positions, open or closed, in one mask period ***d***)	Increased	Increased	No change	Improved	Improved
Pa (mask hole diameter)	Increased	Increased	Deteriorated	Improved	Improved

Mol Imaging Biol. Author manuscript; available in PMC 2013 April 1.

Table 4

Performance of Coded Aperture Masks Optimized for Various Detector Sizes using Sensitivitv/(XY Resolution)^2 as the Figure of Merit.

D (cm)	*b* (cm)	*npm*	*Pa* (mm)	*d* (cm)	2*d* (cm)	*a* (cm)	FOV (cm)	XY Resolution (mm)	Z Resolution (mm)	Sensitivity (%)	Sampling Index
10	50	14	1.20	1.68	3.35	10 (min *a*)	2.01	1.55	18.29	0.0186	5.31
						25 (min *a* + 15 cm)	**2.52**	**2.33**	**77.09**	**0.0031**	**2.67**
						40 (min *a* + 30 cm)	3.02	3.22	189.34	0.0012	2.00
20	50	22	1.52	3.35	6.70	10 (min *a*)	4.02	1.91	11.19	0.0707	6.76
						25 (min *a* + 15 cm)	**5.03**	**2.73**	**40.59**	**0.0124**	**3.39**
						40 (min *a* + 30 cm)	6.04	3.64	93.74	0.0049	2.55
30	36.5	46	1.41	6.48	12.97	10 (min *a*)	8.27	1.96	5.64	0.2162	4.85
						25 (min *a* + 15 cm)	**10.94**	**3.13**	**25.10**	**0.4380**	**2.57**
						40 (min *a* + 30 cm)	13.60	4.41	60.75	0.0179	2.00
40	35	62	1.44	8.93	17.87	10 (min *a*)	11.50	2.03	4.21	0.3446	4.80
						25 (min *a* + 15 cm)	**15.34**	**3.26**	**18.86**	**0.0791**	**2.57**
						40 (min *a* + 30 cm)	19.16	4.61	45.62	0.0331	2.01

Optimization was performed at ***a*** = 25 cm (boldface) and assumed a ^{99m}Tc point source. Performance at min ***a*** (10 cm) and (min ***a*** + 30 cm) are also shown. ***mt*** = 1 mm. ***b*** was varied from 10 to 50 cm, in 0.5 cm increments. ***npm*** was set to 2, 6, 14, 22, 38, 46, 62, 86, 94 or 118. ***Pa*** was calculated for each combination of ***b*** and ***npm*** using the following expression after setting min ***a*** = 10 cm:

$$Pa = D \times \frac{2min\_a + mt}{2npm \times (min\_a + b)}$$

. A sampling index of ≥ 2.0 was maintained during optimization.